

# Direct experimental evidence of physical origin of electronic phase separation in manganites

Tian Miao<sup>a</sup>, Lina Deng<sup>a,1</sup>, Wenting Yang<sup>a,1</sup>, Jinyang Ni<sup>a</sup>, Changlin Zheng<sup>a</sup>, Joanne Etheridge<sup>b</sup>, Shasha Wang<sup>c</sup>, Hao Liu<sup>a</sup>, Hanxuan Lin<sup>a</sup>, Yang Yu<sup>a</sup>, Qian Shi<sup>a</sup>, Peng Cai<sup>a</sup>, Yinyan Zhu<sup>a</sup>, Tieying Yang<sup>d</sup>, Xingmin Zhang<sup>d</sup>, Xingyu Gao<sup>d</sup>, Chuanying Xi<sup>e</sup>, Mingliang Tian<sup>c</sup>, Xiaoshan Wu<sup>e</sup>, Hongjun Xiang<sup>a</sup>, Elbio Dagotto<sup>f,g,2</sup>, Lifeng Yin<sup>a,h,i,2</sup>, and Jian Shen<sup>a,b,i,2</sup>

<sup>a</sup>State Key Laboratory of Surface Physics and Department of Physics, Fudan University, 200433 Shanghai, China; <sup>b</sup>Monash Centre for Electron Microscopy, Monash University, VIC 3800, Australia; <sup>c</sup>Anhui Province Key Laboratory of Condensed Matter Physics at Extreme Conditions, High Magnetic Field Laboratory of the Chinese Academy of Sciences, 230031 Hefei, Anhui, China; <sup>d</sup>Shanghai Synchrotron Radiation Facility, Shanghai Institute of Applied Physics, Chinese Academy of Sciences, 201204 Shanghai, China; <sup>e</sup>Laboratory of Solid State Microstructures, Department of Physics, Nanjing University, 210093 Nanjing, China; <sup>f</sup>Department of Physics and Astronomy, University of Tennessee, Knoxville, TN 37996; <sup>g</sup>Materials Science and Technology Division, Oak Ridge National Laboratory, Oak Ridge, TN 37831; <sup>h</sup>Institute for Nanoelectronics Devices and Quantum Computing, Fudan University, 200433 Shanghai, China; and <sup>i</sup>Collaborative Innovation Center of Advanced Microstructures, 210093 Nanjing, China

Edited by Tsuyoshi Kimura, University of Tokyo, Tokyo, Japan, and accepted by Editorial Board Member Gabriel Aeppli February 19, 2020 (received for review November 20, 2019)

**Electronic phase separation in complex oxides is the inhomogeneous spatial distribution of electronic phases, involving length scales much larger than those of structural defects or nonuniform distribution of chemical dopants. While experimental efforts focused on phase separation and established its correlation with nonlinear responses under external stimuli, it remains controversial whether phase separation requires quenched disorder for its realization. Early theory predicted that if perfectly “clean” samples could be grown, both phase separation and nonlinearities would be replaced by a bicritical-like phase diagram. Here, using a layer-by-layer superlattice growth technique we fabricate a fully chemically ordered “tricolor” manganite superlattice, and compare its properties with those of isovalent alloyed manganite films. Remarkably, the fully ordered manganite does not exhibit phase separation, while its presence is pronounced in the alloy. This suggests that chemical-doping-induced disorder is crucial to stabilize the potentially useful nonlinear responses of manganites, as theory predicted.**

electronic phase separation | manganites | tricolor superlattice | chemical ordering

**C**hemical doping is the most commonly used procedure to induce exotic phenomena, such as superconductivity and colossal magnetoresistance (CMR), in complex oxides (1–5). While the extra charges provided by the chemical dopants are crucial for these phenomena, the dopants themselves are randomly distributed inevitably introducing quenched disorder in the systems (5–8). Theoretically, such disorder has been proposed to have a profound influence on the length scale of electronic phase separation (EPS), especially for CMR manganites (9–14). Experimentally, the investigation of the role of disorder induced by chemical dopants is challenging due to the difficulty of sample fabrication. Superlattice growth with atomic precision has been used before to locate the chemical dopants with periodic spatial order (15–18). In particular, a “bicolor”  $(\text{LaMnO}_3)_{2n}/(\text{SrMnO}_3)_n$  manganite superlattice was prepared in ref. 16. Moreover, in special cases bulk-ordered alloys were formed at half doping (19–21). In ref. 19 a close relation between disorder and CMR was established, but EPS was not studied. In addition, previous investigations by our group observed that the spatial ordering of Pr dopants in a  $(\text{La}_{1-y}\text{Pr}_y)_{1-x}\text{Ca}_x\text{MnO}_3$  (LPCMO) system reduces the length scale of EPS domains by a factor of 10 (22). However, in that study LPCMO remained disordered with regards to the random distribution of Ca dopants. To the best of our knowledge, there has been no direct report on how EPS behaves in a fully chemically ordered manganite. This is important because EPS has been widely related with the CMR properties that render manganites attractive from the fundamental physics

perspective and potentially valuable for applications (23). Moreover, the potential relevance of disorder for functionalities in oxides has been highlighted more broadly as a promising avenue of exploration [see for example the recent study by the US Department of Energy (24)].

In this work, we use LPCMO ( $x = 1/3$ ,  $y = 1/2$ ) thin films as a prototype system to demonstrate how EPS responds to full chemical ordering, i.e., the Pr and the Ca dopants are both spatially ordered. This complete chemical order is achieved by growing 1 unit cell  $\text{LaMnO}_3$  (LMO)/1 unit cell  $\text{PrMnO}_3$  (PMO)/1 unit cell  $\text{CaMnO}_3$  (CMO) tricolor superlattices. Such a superlattice clearly is an example of a fully chemically ordered  $\text{La}_{1/3}\text{Pr}_{1/3}\text{Ca}_{1/3}\text{MnO}_3$  thin film (dubbed O-LPCMO). Strikingly, we observed that while the conventional  $\text{La}_{1/3}\text{Pr}_{1/3}\text{Ca}_{1/3}\text{MnO}_3$  thin-film alloys with random Pr and Ca locations (dubbed R-LPCMO) exhibit pronounced large length-scale EPS of micrometer size, the O-LPCMO exhibits a single phase without any observable EPS. This result is directly obtained by magnetic force microscopy (MFM) and further backed by global physical property measurements. The dramatic absence of EPS in the O-LPCMO system strongly indicates that

## Significance

**We report a breakthrough in addressing a long-standing and challenging issue: the physical origin of electronic phase separation phenomena in complex oxides. Using tricolor monoatomic superlattice growth, we provide direct experimental evidence to show that the chemical-dopants-induced disorder is crucial for electronic phase separation and colossal magnetoresistance effect. Conceptually our results are far reaching: we believe that correlated materials in general likely need deviations from ideality to display the crucial nonlinear effects important for devices.**

Author contributions: J.S. designed research; T.M., L.D., W.Y., J.N., C.Z., J.E., S.W., H. Liu, H. Lin, Y.Y., Q.S., P.C., Y.Z., T.Y., X.Z., X.G., C.X., M.T., and H.X. performed research; T.M., C.Z., J.E., T.Y., X.Z., X.W., H.X., E.D., L.Y., and J.S. analyzed data; and T.M., E.D., L.Y., and J.S. wrote the paper.

The authors declare no competing interest.

This article is a PNAS Direct Submission. T.K. is a guest editor invited by the Editorial Board.

Published under the PNAS license.

<sup>1</sup>L.D. and W.Y. contributed equally to this work.

<sup>2</sup>To whom correspondence may be addressed. Email: edagotto@utk.edu, lifengyin@fudan.edu.cn, or shenj5494@fudan.edu.cn.

This article contains supporting information online at <https://www.pnas.org/lookup/suppl/doi:10.1073/pnas.1920502117/-DCSupplemental>.

First published March 16, 2020.

chemical-doping-induced disordering plays a critical role in EPS phenomena in complex oxides, compatible with early theory predictions (9–14) that only now can be addressed with advances in superlattice fabrication techniques. Our approach can be extended to other doped manganites and complex oxides systems, providing a powerful way to study the influence of chemical ordering on EPS and other physical properties of complex oxides.

Fig. 1A shows schematic views of the crystal structures of the R-LPCMO (*Left*) and the O-LPCMO (*Right*) superlattices. The doped cations (Ca and Pr) distribute randomly in the R-LPCMO, in stark contrast to the fully chemical ordered O-LPCMO system. Fig. 1B shows the in situ reflection high-energy electron diffraction (RHEED) intensity oscillations during the growth process, displaying the alternating unit-cell-by-unit-cell growth of the LMO (red), PMO (yellow), and CMO (blue) layers. By carefully controlling the growth of each atomic layer of the three materials, we managed to prepare a 10-nm-thick  $[(\text{LMO})_1/(\text{PMO})_1/(\text{CMO})_1]_8$  superlattice on a lattice-matched  $\text{NdGaO}_3$  (110) (NGO) substrate. Because of the different lattice constants of LMO, PMO, and CMO, in principle it is a challenge to find a suitable substrate and narrow growth conditions and sequences (“sweet spot”) to minimize the strain energy [for instance, the 105 K structural transition of  $\text{SrTiO}_3$  (100) (25) affects the superlattice structure grown on this substrate irreversibly]. It is our success in growing a stable tricolor manganite superlattice that leads to the understanding of EPS in chemically ordered systems reported here, giving unique characteristics to our project.

The superlattice is of high quality, as proven by the distinct X-ray diffraction (XRD) superlattice peaks (red arrows) in Fig. 1C. Note that the XRD peaks of the superlattice are almost superimposed with those of the substrate, reflecting the fact that the superlattice and the substrate are nearly perfectly lattice matched, thus minimizing lattice distortions. Moreover, we performed X-ray reflection measurements (Fig. 1D, black line) and our fitting results (red dots) in Fig. 1D indicate that the interfaces in the superlattice are sharp (for details see *SI Appendix*).

The high quality of the O-LPCMO film is further supported by transmission electron microscopy (TEM) data. Fig. 1E shows a cross-sectional high angle annular dark-field scanning

transmission electron microscopy (HAADF-STEM) image (*Left*) and the intensity line profile (*Right*) of the marked area in the HAADF-STEM image for the O-LPCMO film. The tricolor superlattice structure can be clearly seen and all of the ordered cations (La, Pr, Ca) can be clearly distinguished in the Z-contrast HAADF-STEM image (Z is the atomic number of the elements) and the intensity profile. A zigzag structure of A sites can be observed for O-LPCMO in the HAADF-STEM image (for details see *SI Appendix*, Fig. S1). The corresponding elemental mapping of La (red), Pr (yellow), and Ca (blue) using integrated intensity of core-loss edges (La  $M_{4,5}$ , Pr  $M_{4,5}$ , and Ca  $L_{2,3}$ ) recorded by electron energy loss spectroscopy (EELS) are shown in Fig. 1F. The trichromatic distribution of the three kinds of cations further indicates the high quality of the superlattice, allowing this reported study of the relationship between EPS and quenched disorder in manganites using a fully ordered sample.

The cation ordering has a dramatic influence on EPS for the LPCMO system. Fig. 2 shows MFM (*SI Appendix*) images acquired under different perpendicular magnetic fields at 10 K after zero-field cooling, as well as transport results at different fields. For the MFM images, the areas with negative-phase signals (red) represent ferromagnetic metallic (FMM) regions, while the areas with zero-phase (white) and positive-phase (blue) signals represent antiferromagnetic charge-ordered insulator (AFM-COI) regions. The MFM images of the R-LPCMO in Fig. 2B show the evolution of EPS with increasing field. Under a 1-T field, the R-LPCMO film exhibits typical large-length-scale EPS of micrometer size. With increasing field at 10 K, the FMM domains grow in size until the film is fully transformed into the ferromagnetic state at 5 T in Fig. 2B. In contrast, the MFM images of the O-LPCMO film in Fig. 3B show no sign of the FMM phase even under a 9-T field, indicating that the system does not display EPS and remains in a single-phase AFM-COI state. We note that changing the stacking sequence from the present LMO/PMO/CMO to LMO/CMO/PMO, the fact that the tricolor superlattices exhibit no signs of EPS still holds, as shown in *SI Appendix*, Figs. S2 and S3. However, if we break the chemical order by annealing, the electron phase separations occur and perform exactly the same as the alloy film (*SI Appendix*, Fig. S4).

Fig. 24 shows the temperature-dependent resistivity ( $R$ - $T$ ) of the R-LPCMO film under different magnetic fields. The cooling

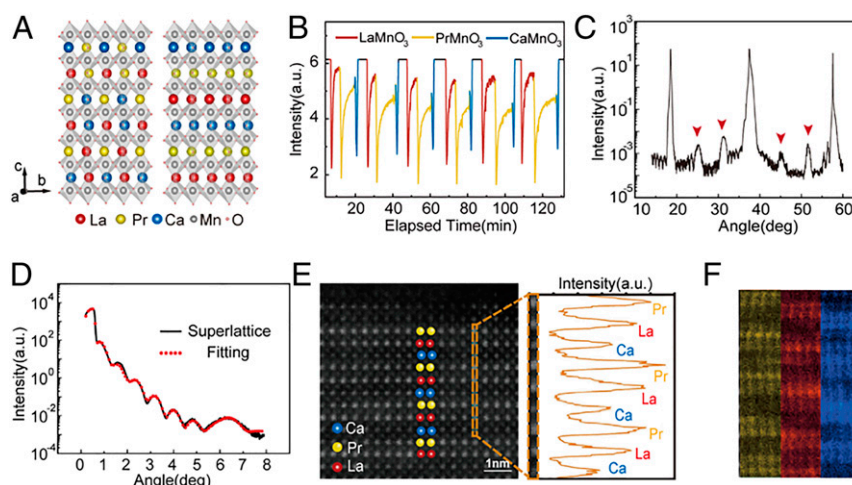


**Fig. 1.** Growth and crystal structure of the ordered  $\text{La}_{1/3}\text{Pr}_{1/3}\text{Ca}_{1/3}\text{MnO}_3$  superlattice film on a  $\text{NdGaO}_3$  (110) substrate. (A) Schematic diagrams of randomly distributed (*Left*) and fully ordered (*Right*) tricolor superlattice manganite systems. Red, yellow, blue, gray, and red spheres represent La, Pr, Ca, Mn, and O atoms, respectively. (B) RHEED oscillations during the layer-by-layer growth process. Red, yellow, and blue lines represent different targets. (C) X-ray diffraction of the 10-nm fully ordered  $\text{La}_{1/3}\text{Pr}_{1/3}\text{Ca}_{1/3}\text{MnO}_3$  film grown on NGO (110) substrate. The red arrows mark the superlattice peaks. (D) Fitting of the X-ray refraction of the fully ordered  $\text{La}_{1/3}\text{Pr}_{1/3}\text{Ca}_{1/3}\text{MnO}_3$  film. The X-ray refraction data are plotted using a black line, while its fitting data use red filled dots. (E) Cross-section HAADF-STEM image of the O-LPCMO film (*Left*) and the Z contrast intensity profile (*Right*) for the dotted line area, which corresponds to the periodic superlattice structure. (F) STEM-EELS mapping of different elements, La (red), Pr (yellow), Ca (blue).

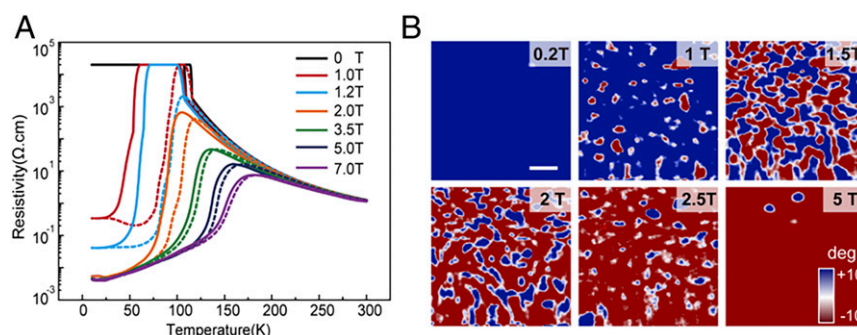


**Fig. 2.** Transport and MFM images of 10-nm R-LPCMO films, grown on NGO (110) substrate at different magnetic fields. (A) The clear CMR effect and huge thermal hysteresis suggests phase separation in the random film, in agreement with previous experimental and theoretical investigations. EPS is also explicitly shown by the MFM images in *B* at different fields and  $T = 10$  K. The magnetic field is applied perpendicular to the film plane. The resistance is measured by the four-point method. MFM was conducted in a tapping mode. (Scale bar in *B*, 2  $\mu\text{m}$ ; color bar for *B*,  $\pm 10^\circ$ .)

(solid lines) and warming (dotted lines) curves exhibit large thermal hysteresis indicating that the 10-nm R-LPCMO thin film on the NGO (110) substrate has a pronounced EPS. For the O-LPCMO film in Fig. 3*A*, on the other hand, the  $R$ - $T$  curves show that the film is always in an insulating state with almost no thermal hysteresis even under 9-T field. This is fully consistent with the observation of MFM images. Resistance values greater than  $2.2 \times 10^4 \Omega\cdot\text{cm}$  are plotted as a constant in Figs. 2*A* and 3*A* representing the fact that the data are out of the measurement range.

Fig. 4*A* and *B* show the changes of resistivity under sweeping magnetic fields for R-LPCMO and O-LPCMO, respectively. The films are first zero-field cooled to a low temperature, and resistivity is measured when the magnetic field is swept from zero to a predesignated value and back to zero. The resistivity is continuously recorded after the field is swept back to zero in order to analyze the time-dependent behavior of the films after the field cycle. This procedure is repeated with a higher predesignated field until the lowest resistivity is reached, i.e., until the films are in the full FMM state.

For the R-LPCMO film (Fig. 4*A*), the resistivity decreases continuously with increasing field at 10 K. After reaching the predesignated field, the field sweeping stops but the resistivity keeps dropping to a stable value (vertical portions of the graphs), which then stays almost unchanged during the period when the field is reduced back to zero, and remains locked at that value with further increasing time. Because the R-LPCMO film is in an EPS state (Fig. 2), the fact that the resistivity remains stable even at zero field indicates that the EPS state is highly stable at 10 K. The lowest possible resistivity appears to be reached when the predesignated limiting field is set to 3 T, as indicated by the fact that the resistivity shows a tendency toward a saturation value

which does not drop further when the field is kept at 3 T or reduced to zero.

The field dependence of the resistivity of the O-LPCMO film is drastically different from that of the R-LPCMO. Fig. 4*B* shows the resistivity measured at 0.38 K under high magnetic field for the O-LPCMO film (At 10 K, the resistance is always out of range, even if in 38 T.) The predesignated field is set to 18 T and higher, in order to allow the resistivity to drop within our measurable range. The lowest possible resistivity appears to be reached when the predesignated field is set to 30 T or higher, as indicated by the tendency toward a saturation value which has the same order of magnitude as that of the R-LPCMO. However, the resistivity of the O-LPCMO keeps increasing during the process when the field is reduced to zero. Once zero field is reached, it takes only a few more seconds for the resistivity to reach its initial value before the application of the magnetic field, as shown by the dotted lines. Apparently, the high-magnetic-field-induced FMM phase is not stable, and the O-LPCMO system prefers a single-phase AFM-COI state. This implies that the EPS state, with coexisting AFM-COI and FMM clusters, is not stable in the fully ordered system O-LPCMO. This is in good agreement with our first-principles calculations which show that the AFM-COI state is the ground state for the O-LPCMO system (for details see *SI Appendix*).

Having identified the drastically different EPS behavior between the fully chemically ordered LPCMO and the conventional LPCMO random alloy, we now turn to discuss the physical origin of EPS in the LPCMO system. The parent compound of LPCMO is LMO, which is an antiferromagnetic insulator. Doping the LMO by Ca provides extra holes and tends to transform the system into a ferromagnetic metallic state (26–28).

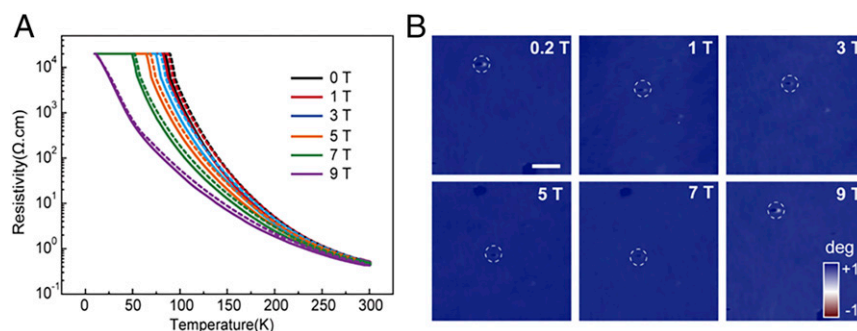


**Fig. 3.** Transport and MFM images of 10 nm O-LPCMO films, grown on NGO (110) substrate at different magnetic fields. (A) The full O-LPCMO film is always insulating and displays almost no thermal hysteresis, quite different from the random film. The MFM image of O-LPCMO in *B* shows no phase separation signal. (Scale bar in *B*, 5  $\mu\text{m}$ ; color bar for *B*,  $\pm 1^\circ$  deg.) The test conditions were the same as in Fig. 2.



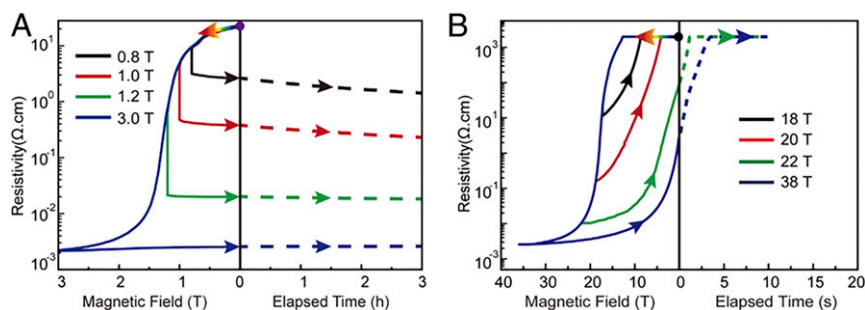


**Fig. 4.** Low-temperature magnetoresistance after zero-field cooling. The solid arrows mark the field-sweeping process, while the dotted arrows indicate the evolution of film resistance over time. After a certain time, the film is heated up to 300 K and then dropped to 10 K to reach the stable state again. (A) Magnetoresistance of the R-LPCMO film at 10 K after zero-field cooling. The resistance first decreases with increasing field. When the field reaches a certain value at which it is held constant, the resistance first continues decreasing to a stable state, and then becomes almost constant with decreasing field. The resistance is approximately constant even after the magnetic field drops to zero for a few hours, as the dotted arrows indicate. (B) Same process as in A but for the O-LPCMO film at 0.38 K. Here with decreasing field the resistance first increases and then returns to the initial state value after a few seconds when the field becomes zero. Note that the measurements of R-LPCMO and O-LPCMO films are carried out in two different magnet systems (*SI Appendix*).

However, the Ca doping also introduces strong chemical disorder in  $\text{La}_{1-x}\text{Ca}_x\text{MO}_3$  (LCMO), leading to nanoscale EPS (29–32). Further doping Pr into LCMO (isovalent substitution of La by Pr) enhances the fluctuations of the competing orders and modifies carrier bandwidths, which is known to induce unusually large micrometer-scale EPS in the R-LPCMO system (3, 4, 33). For the O-LPCMO case, because all cations are spatially ordered, the dopants-induced quenched disorder no longer exists and there are no seeding locations for EPS clusters even if the competing states are close in energy. The system will stay in a single-phase state, which is observed and calculated to be the AFM-COI state. Note that the O-LPCMO system transits to the FMM state under magnetic fields  $\sim 30$  T. Although such a magnetic field can drive the system into the FMM state, it is unstable and will recover its AFM state once the field is switched off.

The reported results are compatible with theoretical predictions formulated over a decade ago (9–14), and confirmed by experiments (34), reproduced as a sketch in Fig. 5. In the clean limit (Fig. 5A) it was predicted that increasing the averaged ionic radius

of the perovskite A-site cations  $r_A$ —which is proportional to the bandwidth of the carriers at constant electronic density—will lead to bicritical behavior between the competing AFM-COI and FMM phases. When the averaged  $r_A$  is reduced this allows the bonds Mn–O–Mn to bend, reducing the Mn–Mn hopping for the  $e_g$  electrons and thus reducing the bandwidth. This prediction was confirmed experimentally using bulk  $\text{RE}_{1-x}\text{AE}_x\text{MnO}_3$  compounds (34). Our superlattice O-LPCMO is located in this phase diagram in the AFM-COI region. On the other hand, by increasing disorder strength, as in R-LPCMO, via an increase in the ionic radii variance, first of all of the critical temperatures are depleted. In our study we estimate that the difference in critical temperatures leading to the AFM-COI state between O-LPCMO and R-LPCMO is  $\sim 60$  K. This depletion is more prominent near the original first-order transition. The temperature range between the clean and “dirty” critical temperatures contains coexisting clusters of both phases, leading to an EPS that induces nonlinear responses such as the CMR (9–14). Note that previous Monte Carlo investigations showed that the AFM-COI phase is particularly

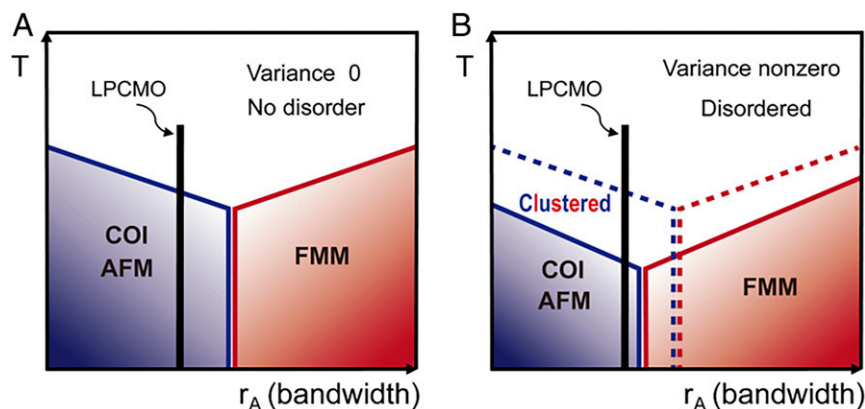


**Fig. 5.** Schematic representation of the theoretical scenario compatible with our experiments. (A) Shown in red and blue solid lines is the idealized ordered clean-limit  $T$ - $r_A$  phase diagram showing how the FM metal and AFM-COI insulator phases compete varying temperature  $T$  and the averaged ionic radius of the perovskite A-site cations,  $r_A$ , that regulates the bandwidth after isovalent chemical doping (9, 10, 34). This theoretical prediction was confirmed by experimental results (34). This panel is at ionic radii variance 0 indicating the ordered state, following ref. 34. The vertical black bar suggests the possible position of our material of focus, O-LPCMO, the ordered superlattice  $\text{La}_{1/3}\text{Pr}_{1/3}\text{Ca}_{1/3}\text{MnO}_3$ , compatible with its CO insulating state at low temperature. (B) Results in the presence of disorder, i.e., for a nonzero ionic variance. In dashed red and blue lines is the clean-phase diagram of A, as reference. The solid lines indicate the phase diagram after adding disorder. Note that according to ref. 34 not only the critical temperatures are suppressed by disorder, as expected, but the transition at  $T = 0$  shifts to the left in real materials. The ground state of R-LPCMO is close to the transition COI-FMM and a small magnetic field can alter the balance, as found experimentally. Upon cooling, the system first travels through a “clustered” region with coexisting CO and FMM small domains, pinned by local fluctuations in the disorder strength (9, 10), and with insulating behavior. This is the  $T$  range between the clean and dirty critical temperatures. Upon further cooling, a transition to the COI (FMM) is reached at zero (nonzero) magnetic field, as in our R-LPCMO sample.

fragile upon the introduction of disorder (35). In excellent agreement with experiments (34) this suggests that the resulting disordered phase diagram in Fig. 5B should be asymmetric, with a shift to the left in Fig. 5B of the original zero-temperature AFM-FM phase transition. This locates R-LPCMO much closer to that AFM-FM transition, making it much easier to destabilize via magnetic fields, as we have observed, transforming R-LPCMO from AFM-COI to FMM.

In summary, we have achieved full chemical ordering in an LPCMO system by growing a high-quality tricolor superlattice. While the conventional LPCMO random alloy has pronounced large-length-scale EPS (and concomitant CMR effects), the full chemically ordered LPCMO system exhibits no sign of EPS. Both experimental measurements and theoretical calculations show that the O-LPCMO system has an AFM-COI ground state. Our study provides direct evidence that the disorder induced by isovalent chemical doping plays the decisive role in stabilizing EPS in the LPCMO system. Since EPS of different length scales from micrometer to nanometer has been extensively associated with the CMR phenomena, our results are compatible with the conjecture proposed by theory over a decade ago that disorder is required as a seed for CMR (9–14). Thus, one of the most widely discussed phenomena in correlated systems, the exciting nonlinear CMR effect with potential device applications, does not appear in clean systems. More generally, as with doped semiconductors that rely on doping impurities to achieve their useful properties, evidence is

accumulating that complex oxides also fundamentally alter their characteristics and responses to external stimuli by the presence of crystal randomness, showing that quenched disorder is more a friend than foe for functionalities.

**Data Availability Statement.** All data discussed in the paper will be made available to readers.

**ACKNOWLEDGMENTS.** We acknowledge W.-B. Wang and X.-D. Zhou for discussions. E.D. thanks Jian Liu for useful conversations. This work was supported by National Key Research and Development Program of China (Grant 2016YFA0300702); National Basic Research Program of China (973 Program) (Grant 2014CB921104); National Natural Science Foundation of China (Grant 11991060); Shanghai Municipal Natural Science Foundation (Grants 18JC1411400, 18ZR1403200, 17ZR1442400, and 17ZR1442600); the Program of Shanghai Academic Research Leader (Grant 18XD1400600); China Postdoctoral Science Foundation (Grants 2017M610221, KLH1512080, and KLH1512089); Shanghai Municipal Natural Science Foundation (Grant 17ZR1442600) and the China Postdoctoral Science Foundation (Grants 2016M601488, 2017T100265); Shanghai Sailing Program (Grant 17YF1429000); and the National Postdoctoral Program for Innovative Talents. E.D. was supported by the US Department of Energy, Office of Science, Basic Energy Sciences, Materials Sciences and Engineering Division. The TEM work was conducted at the Monash Centre for Electron Microscopy using an instrument funded by Australian Research Council's Linkage Infrastructure, Equipment and Facilities Grant No. LE0454166. A portion of this work was performed on the Steady High Magnetic Field Facilities, High Magnetic Field Laboratory, CAS.

1. P. A. Lee, N. Nagaosa, X. G. Wen, Doping a Mott insulator: Physics of high-temperature superconductivity. *Rev. Mod. Phys.* **78**, 17–85 (2004).
2. M. Fäth *et al.*, Spatially inhomogeneous metal-insulator transition in doped manganites. *Science* **285**, 1540–1542 (1999).
3. M. Uehara, S. Mori, C. H. Chen, S. W. Cheong, Percolative phase separation underlies colossal magnetoresistance in mixed-valent manganites. *Nature* **399**, 560–563 (1999).
4. D. N. Argyriou *et al.*, Glass transition in the polaron dynamics of colossal magnetoresistive manganites. *Phys. Rev. Lett.* **89**, 036401 (2002).
5. E. Dagotto, Complexity in strongly correlated electronic systems. *Science* **309**, 257–262 (2005).
6. Y. Dubi, Y. Meir, Y. Avishai, Nature of the superconductor-insulator transition in disordered superconductors. *Nature* **449**, 876–880 (2007).
7. Y. Motome, N. Furukawa, N. Nagaosa, Competing orders and disorder-induced insulator to metal transition in manganites. *Phys. Rev. Lett.* **91**, 167204 (2003).
8. Y. Tokura, N. Nagaosa, Orbital physics in transition-metal oxides. *Science* **288**, 462–468 (2000).
9. A. Moreo, M. Mayr, A. Feiguin, S. Yunoki, E. Dagotto, Giant cluster coexistence in doped manganites and other compounds. *Phys. Rev. Lett.* **84**, 5568–5571 (2000).
10. J. Burgu, M. Mayr, V. Martin-Mayor, A. Moreo, E. Dagotto, Colossal effects in transition metal oxides caused by intrinsic inhomogeneities. *Phys. Rev. Lett.* **87**, 277202 (2001).
11. J. Burgu, A. Moreo, E. Dagotto, Relevance of cooperative lattice effects and stress fields in phase-separation theories for CMR manganites. *Phys. Rev. Lett.* **92**, 097202 (2004).
12. E. Dagotto, T. Hotta, A. Moreo, Colossal magnetoresistant materials: The key role of phase separation. *Phys. Rep.* **344**, 1–153 (2001).
13. C. Shen, G. Alvarez, E. Dagotto, Insulator-to-metal transition induced by disorder in a model for manganites. *Phys. Rev. B Condens. Matter Mater. Phys.* **70**, 64428 (2004).
14. C. Shen, G. Alvarez, E. Dagotto, Competing ferromagnetic and charge-ordered states in models for manganites: The origin of the colossal magnetoresistance effect. *Phys. Rev. Lett.* **98**, 127202 (2007).
15. S. J. May *et al.*, Enhanced ordering temperatures in antiferromagnetic manganite superlattices. *Nat. Mater.* **8**, 892–897 (2009).
16. A. Bhattacharya *et al.*, Metal-insulator transition and its relation to magnetic structure in  $(\text{LaMnO}_3)_{2n}/(\text{SrMnO}_3)_n$  superlattices. *Phys. Rev. Lett.* **100**, 257203 (2008).
17. S. Smadici *et al.*, Electronic reconstruction at  $\text{SrMnO}_3$ - $\text{LaMnO}_3$  superlattice interfaces. *Phys. Rev. Lett.* **99**, 196404 (2007).
18. J. Seo, B. T. Phan, J. Stahn, J. Lee, C. Panagopoulos, Relaxor characteristics at the interfaces of  $\text{NdMnO}_3/\text{SrMnO}_3/\text{LaMnO}_3$  superlattices. *Phys. Rev. B Condens. Matter Mater. Phys.* **82**, 140405 (2010).
19. D. Akahoshi *et al.*, Random potential effect near the bicritical region in perovskite manganites as revealed by comparison with the ordered perovskite analogs. *Phys. Rev. Lett.* **90**, 177203 (2003).
20. N. C. Bristowe, J. Varignon, D. Fontaine, E. Bousquet, P. Ghosez, Ferromagnetism induced by entangled charge and orbital orderings in ferroelectric titanate perovskites. *Nat. Commun.* **6**, 6677 (2015).
21. A. Brinkman *et al.*, Magnetic effects at the interface between non-magnetic oxides. *Nat. Mater.* **6**, 493–496 (2007).
22. Y. Zhu *et al.*, Chemical ordering suppresses large-scale electronic phase separation in doped manganites. *Nat. Commun.* **7**, 11260 (2016).
23. K. Lai *et al.*, Mesoscopic percolating resistance network in a strained manganite thin film. *Science* **329**, 190–193 (2010).
24. US Department of Energy, Office of Science, Quantum Materials for Energy Relevant Technology, February 2016. [https://science.osti.gov/-/media/bes/pdf/reports/2016/BRNQM\\_rpt\\_Final\\_12-09-2016.pdf?la=en&hash=E7760711641883FFC9F110D70385937D6A31C64F](https://science.osti.gov/-/media/bes/pdf/reports/2016/BRNQM_rpt_Final_12-09-2016.pdf?la=en&hash=E7760711641883FFC9F110D70385937D6A31C64F). Accessed 1 February 2020.
25. F. Lan *et al.*, Observing a previously hidden structural-phase transition onset through heteroepitaxial cap response. *Proc. Natl. Acad. Sci. U.S.A.* **116**, 4141–4146 (2019).
26. P. Schiffer, A. P. Ramirez, W. Bao, S. W. Cheong, Low temperature magnetoresistance and the magnetic phase diagram of  $\text{La}_{1-x}\text{Ca}_x\text{MnO}_3$ . *Phys. Rev. Lett.* **75**, 3336–3339 (1995).
27. S. Jin *et al.*, Thousandfold change in resistivity in magnetoresistive  $\text{La-Ca-Mn-O}$  films. *Science* **264**, 413–415 (1994).
28. K. I. Chahara, T. Ohno, M. Kasai, Y. Kozono, Magnetoresistance in magnetic manganese oxide with intrinsic antiferromagnetic spin structure. *Appl. Phys. Lett.* **63**, 1990–1992 (1993).
29. J. M. Zuo, J. Tao, Nanometer-sized regions of charge ordering and charge melting in  $\text{La}_{2/3}\text{Ca}_{1/3}\text{MnO}_3$  revealed by electron microdiffraction. *Phys. Rev. B Condens. Matter Mater. Phys.* **63**, 60407 (2001).
30. V. Kiryukhin, T. Y. Koo, H. Ishibashi, J. P. Hill, S. W. Cheong, Average lattice symmetry and nanoscale structural correlations in magnetoresistive manganites. *Phys. Rev. B Condens. Matter Mater. Phys.* **67**, 64421 (2003).
31. J. Tao *et al.*, Direct imaging of nanoscale phase separation in  $\text{La}_{0.55}\text{Ca}_{0.45}\text{MnO}_3$ : Relationship to colossal magnetoresistance. *Phys. Rev. Lett.* **103**, 97202 (2009).
32. C. Israel *et al.*, Translating reproducible phase-separated texture in manganites into reproducible two-state low-field magnetoresistance: An imaging and transport study. *Phys. Rev. B Condens. Matter Mater. Phys.* **78**, 54409 (2008).
33. W. Wu *et al.*, Magnetic imaging of a supercooling glass transition in a weakly disordered ferromagnet. *Nat. Mater.* **5**, 881–886 (2006).
34. Y. Tomioka, Y. Tokura, Global phase diagram of perovskite manganites in the plane of quenched disorder versus one-electron bandwidth. *Phys. Rev. B Condens. Matter Mater. Phys.* **70**, 14432 (2004).
35. G. Alvarez, H. Aliaga, C. Shen, E. Dagotto, Fragility of the A-type AF and CE phases of manganites: Insulator-to-metal transition induced by quenched disorder. *Phys. Rev. B Condens. Matter Mater. Phys.* **73**, 224426 (2006).